Photoacoustic tissue characterization using envelope statistics and ultrasonic spectral parameters

Eno Hysi, Dustin Dopsa, Michael C. Kolios

Department of Physics, Ryerson University, Toronto, Ontario, Canada
mkolios@ryerson.ca

ABSTRACT

Photoacoustic (PA) tissue characterization relies on the analysis of ultrasound (US) signals generated through the PA effect. The probability distributions of PA signal amplitude as well as the frequency content of the PA signals are typically not considered. We present a phantom study where we introduce the combined use of US/PA signal envelope statistics along with analysis of the frequency content of the US/PA signals for the purposes of monitoring physical changes in the absorbers. The phantoms were constructed using black polystyrene beads (radius 1.77 μm and 7.36 μm). Tissue microenvironment was emulated by homogenously mixing 10 beads/imaging-transducer-resolution-volume in order to accommodate large numbers of sub-resolved beads. The phantoms were imaged with the Vevo LAZR US/PA integrated imaging system (Fujifilm-VisualSonics) using a 40 MHz linear array probe and 680 nm illumination. US/PA signals from the same region of interest were analyzed by mapping the signal amplitudes distributions from 5 phantom locations, fitting the data to the Generalized Gamma (GG) distribution and extracting the fit parameters while computing the normalized power spectra to retrieve the spectral slope (SS) and midband fit (MBF) spectral parameters. The GG scale parameter increased by 500x for US images and 12x for PA equivalents as the size of the beads increased by ~4.5x. The SS decreased by 0.8x for US and 0.4x for PA. These changes can be attributed variations in size and spatial organization of the beads suggesting that combined US/PA statistical and spectral analysis can potentially monitor normal and abnormal tissue physiological changes.

Keywords: Photoacoustic imaging, Quantitative photoacoustic imaging, Quantitative ultrasound imaging, Envelope statistics, Radiofrequency spectroscopy, Tissue characterization

1. INTRODUCTION

Photoacoustic (PA) images are critically dependent on the method of acquisition, in particular on the choice of the optical illumination wavelengths, geometry and the choice of ultrasonic parameters used for the detection of the PA waves. Excellent imaging of the vasculature has been achieved using PA imaging, making it one of the most active modalities in biomedical imaging research [1]. This has enabled the exploration of a wide range of applications in biomedicine from the imaging of the pathologies of single red blood cells (RBCs) [2] and microvasculature [3] using the endogenous contrast of hemoglobin to the contrast enhanced imaging of tumor microenvironment using biomarkers such as nanoparticles for the visualization of carcinomas [4], [5]. Preclinical PA imaging has been made possible by the advances of fully integrated US/PA or PA imaging systems (custom-made and commercial) whose *in-vivo* applications span a range of disciplines from cancer detection [6], functional assessment of oxygen saturation [7] and dynamic imaging of pharmacokinetics and bio distributions [8]. Attempts for the translation of PA imaging from bench-to-bed-side have mainly focused on the imaging of breast carcinomas [9], [10] but have yet to make a significant impact due to the complexity of the images generated and difficulties in their interpretation.

Translation of PA imaging into mainstream radiology will likely depend on whether PA imaging can provide co-registered structural (i.e. anatomical) and functional (i.e. metabolic) information on the tissue or organ of interest. Due to the endogenous contrast of blood hemoglobin, it is reasonable to expect that a practical use of PA imaging can be the determination of changes in gross anatomical vascular structures due to numerous pathologies, the most obvious being tumor angiogenesis [11]. However, almost all conventional PA images generated rely on displaying the envelope-detected amplitude of the radio-frequency (RF) signals (recorded by an ultrasonic transducer with a finite frequency bandwidth) as brightness pixels. This not only renders the acquisition heavily dependent on the user-defined settings

Photons Plus Ultrasound: Imaging and Sensing 2014, edited by Alexander A. Oraevsky, Lihong V. Wang,
Proc. of SPIE Vol. 8943, 89432E · © 2014 SPIE · CCC code: 1605-7422/14/$18 · doi: 10.1117/12.2038624

(both from the optical illumination and ultrasonic detection point of view) but also on the frequency bandwidth of the transducer that will define the resolution volume of the system. With the exception of easy-to-reach optical targets (i.e. small animal ears or brains), optical illumination must be unfocused in order to capture deeper, clinically relevant regions of interest (ROIs) [12].

More often than not, the tissue imaging resolution volume contains many sub-resolution sources (scatterers of sound and absorbers of light) and relying on RF-amplitude-brightness-generated-images to quantify changes in tissue structure/composition can be difficult to interpret. At clinically relevant ultrasonic frequencies (< 30 MHz), US/PA images of tissue appear to contain speckle, primarily due to the wave interference pattern resulting from the proximity of the scatterers/absorbers [13]. Speckle is considered universal among all coherent imaging modalities (i.e. laser and US) and often does not correspond to the real structure of the tissue examined but rather a representation of the geometrical distribution of scatterers/absorbers. In US imaging, the presence of speckle is considered both detrimental to the spatial resolution of images and beneficial for the purposes of ultrasound tissue characterization (UTC). UTC methods involve the analysis of both the spatial and frequency content of the US RF signals detected from band limited transducers [14], [15]. In the time/spatial domain, the amplitude of the envelope of the RF signals has a statistical distribution which is determined by the spatial organization of the scatterers as well as their physical size and concentration. Various distributions can be employed to differentiate between different tissue types on the assumption that the scattering strength and spatial organization of scatterers determines the fit parameters of the distribution. In the frequency domain, the physical properties such as the size, density and concentration of scatterers affect the frequency content of the RF signals and spectral parameters such as the spectral slope (SS) and midband fit (MBF) can be used to monitor changes in these properties. These methods of analysis have given rise to the field of quantitative ultrasound (QUS) [16], with clinical applications in the detection and characterization of cancer and the subsequent response to therapy [17].

PA imaging, by virtue of its ability to produce ultrasonic waves following laser illumination, is prone to the same speckle phenomena present in US imaging. The source of speckle in PA tissue imaging will primarily be the interference pattern of the most abundant optical absorbers within the US resolution volume, for example RBCs confined within vascular networks which are typically not resolvable in the clinical frequency regime. It is thus expected that the spatial distribution and physical properties of optical absorbers will dictate the statistics of the PA RF signal envelope and their frequency content [18]. Quantitative photoacoustics (QPA) requires a fundamental understanding of the physics of PA wave generation in tissue. Single cell experiments with PA microscopy [2], [19] have shown that frequency analysis of the PA RF signals provide excellent insight into the origin of the PA signals from RBCs and vessels. Transitioning towards clinical frequencies has been guided by studying the PA signal frequencies in collections of RBCs and their pathologies [20], [21]. The current study attempts to investigate the potential of QPA as a method for tissue characterization and treatment monitoring at clinically relevant frequencies. Studies with tissue mimicking phantoms can help aid in the interpretation of clinical data involving PA imaging.

2. METHODS

2.1 Construction of tissue-mimicking phantoms

Phantoms were prepared by combining type-B gelatin powder derived from porcine skin (Sigma-Aldrich Co., St. Louis, MO) with degassed water. The scatterers/absorbers used were monodisperse, black polystyrene beads (Merck Millipore, Pithiviers, France) with diameters of 3.5 μm and 14.72 μm. The physical and acoustical properties of the two phantoms constructed are summarized in Table 1. The diameters of the beads were chosen in order to target two different types of ultrasound scattering regimes, Rayleigh and Faran scattering. The scattering regime is primarily determined by the relationship between the size of the scattering object (i.e. the bead) and the frequency of the incident pressure wave (i.e. the frequency of the US imaging transducer, 40 MHz). The scattering cross-section of each bead was calculated by using the expression for the ultrasonic scattering of a rigid spherical scatterer:

$$\sigma_s = \frac{7\pi k^4 a^6}{9} \tag{1}$$

where, $k=2\pi/\lambda$ is the wave number for the incident US wave with wavelength λ and a is the radius of the scatterer [13].

In order to construct each phantom, degassed water was heated to 35 °C along with the beads before the gelatin powder (10% w/v concentration) was slowly added while magnetic stirring was constantly maintained. The bead-gelatin-water

suspension was stirred to achieve homogeneity until it reached 65 °C to ensure the gelatin was entirely dissolved. The suspension was then added to a rectangular mold (40 mm x 60 mm x 15 mm) and placed inside a custom-made rotisserie for 3 hours at room temperature to ensure homogenous mixing of the beads inside each phantom. After 3 hours, each phantom was kept at 4 °C for 24 hours prior to imaging in order to achieve full solidification of the gelatin.

Table 1. Properties of US/PA phantoms.

Phantom / Properties	Rayleigh	Faran
Radius – a (μm)	1.77	7.36
US wave number – k (μm^{-1})	0.16	0.16
US ka	0.28	1.18
US scattering cross-section – σ (μm^2)	0.05	275.5
Bead density – ρ (g/cm^3)	1.05	1.05
Beads/US resolution volume – (#/μm^3)	10	10
Beads/ phantom – (#)	3.3e12	6.3e8

2.2 US/PA imaging setup

A schematic of the US/PA imaging system used to image the tissue-mimicking phantoms is shown in figure 1. The integrated US/PA system, the Vevo LAZR, was developed by Fujifilm VisualSonics (Toronto, Canada). It consisted of a linear array transducer (256 elements, 40 MHz center frequency) coupled to a tunable Nd:YAG laser (680-970 nm) with a 20 Hz pulse repetition rate, 10 ns pulse width and 30 mJ pulse energy. The optical source was delivered through an optical fiber bundle terminating with two 20 x 1.25 mm strips located along both sides of the acoustic aperture emitting two laser beams at an angle of 30° relative to the US imaging plane. The axial, lateral and elevational resolutions for transducer were 40 μm, 95 μm and 154 μm, respectively, which determined the resolution volume of the probe operating at 40 MHz transmit frequency (5.54e-4 mm^3). The transducer frequency response was measured by using Plexiglas and a 200 nm thick gold film for US and PA modes, respectively. The Plexiglas provide the two-way pulse-echo response of the transducer in US mode while the gold film produces a broadband PA signal which provides a flat PA spectral response over the usable bandwidth of the transducer in receive mode.

For US/PA imaging, each phantom was immersed in a degassed water bath to ensure acoustic coupling with the US/PA transducer. The laser operated at 680 nm. To ensure that each phantom was homogenous with regards to the bead distribution, the probe was scanned over 5 different, random locations in the phantom and 2D, co-registered US/PA B-mode images were collected.

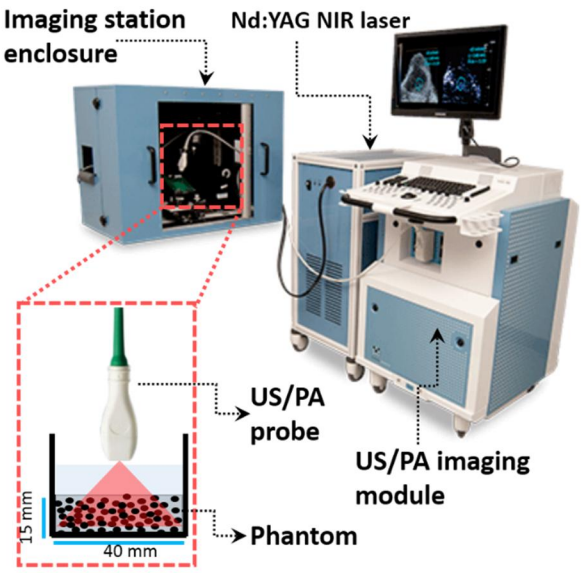

Figure 1. Vevo LAZR integrated US/PA imaging system (Fujifilm VisualSonics) used to image the tissue-mimicking phantoms with black polystyrene beads.

2.3 Computing envelope statistics and ultrasonic spectral parameters

Upon extraction of the US and PA RF signals through in-phase and quadrature sampling, the data was exported in Matlab 2013b (Mathworks Inc., Natick, MA) where it was beamformed. All subsequent analysis was performed using in-house written software. The US B-mode images were used to select an ROI around the transducer field of view (~8-13 mm). The same ROI was then applied to the corresponding, co-registered PA image across 5 different views for each phantom. This was done to assess the homogeneity of each phantom.

The histograms of the signal envelope amplitudes were computed for each frame for all the US/PA RF signals from within a selected ROI. The Generalized Gamma probability density function (GG PDF) was then fitted to the histogram using an implementation of the Maximal Likelihood Estimation routine [15]. This is an iterative process which uses the Neider-Mead Simplex method to optimize the fit. Two fit parameters, a scale parameter (*GG a*) and a shape parameter (*GG c/v*) were extracted and the Kolmogorov-Smirnov (KS) goodness of fit test was used to assess the ability of the GG PDF to provide a fit for the data. A KS critical value (CV) less than $1.36/N^{0.5}$, was used to accept the fit model for a significance level of 5%, where N is the sample size. An unpaired t-test was used to establish the statistical significance ($p < 0.05$) in the comparison of the US/PA GG fit parameters for the Rayleigh and Faran.

For the extraction of ultrasonic spectral parameters, namely the SS and MBF, the power spectra from each RF line within the ROI was computed, normalized by the respective reference (Plexiglas for US and gold film for PA) and averaged across the entire ROI and across all 5 phantom locations. The normalized spectrum within the -6 dB bandwidth of the transducer (US: 12.1-32.8 MHz, PA: 7.6-48 MHz) was then fitted to a straight line. The SS and MBF for each frame were computed and averaged. An unpaired t-test was used to establish statistical significance ($p < 0.05$) in the comparison of the US/PA SS and MBF for the Rayleigh and Faran phantoms.

3. RESULTS AND DISCUSSION

3.1 Co-registered US/PA images

A representative US and PA image for each of the phantoms is shown in figure 2. A common feature of both US and PA images for both phantoms is the presence of speckle. The Faran phantom contains beads which have greater scattering cross-sections compared to the Rayleigh phantom, as seen from the overall increase in the intensity (~10 dB) of the B-

mode images (figures 2(a), (b) vs. figures 2(d), (e)). The same trend can be observed from the PA images (figures 2(c) vs. 2(f)). The increase in US/PA signal amplitudes can also be attributed to the greater (~5000x) scattering cross section of the Faran beads compared to the Rayleigh beads as shown in table 1. Even though the Rayleigh phantom contains more beads per unit volume than the Faran phantom due to the difference in bead size, the US backscatter is stronger for the Faran phantom due to the size of the beads being nearly 4.5 times greater. This difference in the size of the beads contributed also to the increase in PA signal strength for the Faran phantom. It is well known that the size of PA absorbers dictates the strength of the PA signal as predicted by theory [18] and confirmed by experiments with single and suspended RBCs [2], [20].

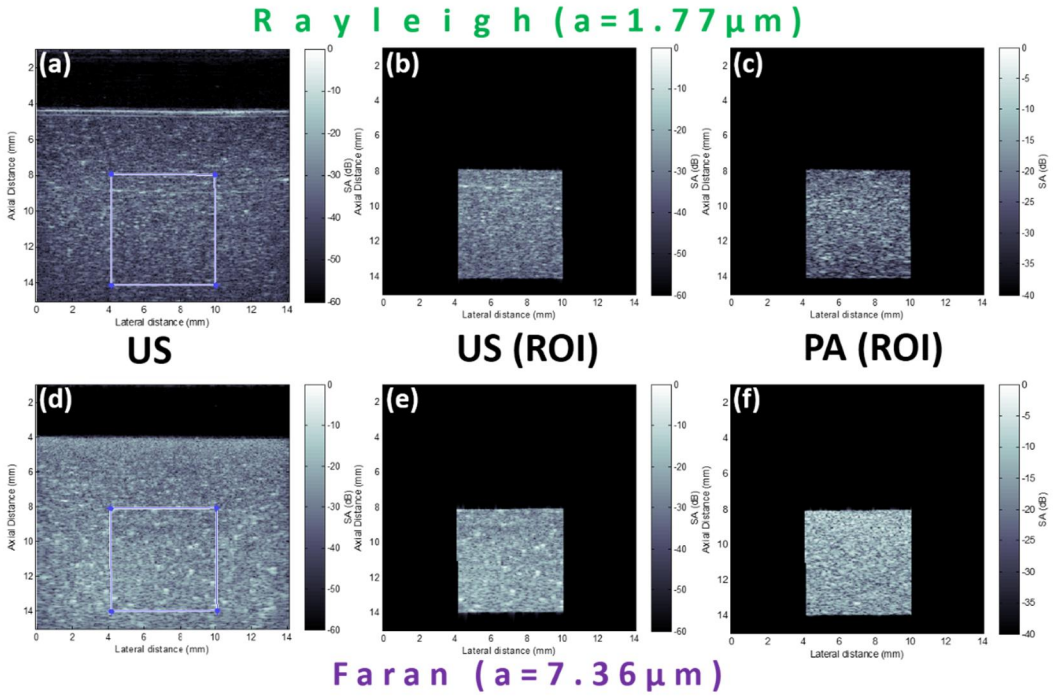

Figure 2. Representatives of the co-registered US/PA images of the Rayleigh (top) and Faran (bottom) phantoms. (a), (d) US B-mode images of the entire phantoms. (b), (e) US B-mode images from the ROI used for analysis. (c), (f) PA B-mode images from the ROI used for analysis. The color bar represents the amplitude of the US and PA signals plotted in a logarithmic scale.

3.2 Envelope statistics

Figure 3 shows the GG fit to the US and PA signal envelope histograms for both the Rayleigh and Faran phantoms. The summary of the fit parameters and the KS goodness of fit test value are shown in table 2. The GG PDF fits relatively well to the envelope histograms for both US and PA signals (figures 3(a) and 3(b)). This is confirmed by the KS goodness of fit test value which for all cases was smaller than the CV, as shown in table 2 for a significance level of 0.05. The GG model is typically used to describe scattering conditions where the medium contains a large number of randomly oriented scatterers with phases randomly distributed between 0 and 2π [15], as was the case with the constructed phantoms.

The GG distribution has been successful in classifying human skin layers using high frequency US *in-vivo* [22] as well as for monitoring structural changes that occur due to chemotherapeutic treatments of cell pellets and preclinical models [23]. The fit parameters for the GG model have the potential to be used as a monitoring tool for assessing the changes that occur in a scattering medium which are not apparent from US/PA B-mode images. In the current study, the US/PA scale (*GG a*) and shape parameter (*GG c/v*) followed the same trends for the Rayleigh and Faran phantoms. Specifically, both parameters were statistically significantly higher for the Faran phantom compared to the Rayleigh phantom ($p<0.05$) and were quite similar within the same phantom as shown by the small standard deviation on the mean (table 3). In the case of the US imaging of the phantoms, the *GG a* parameter for the Faran phantom was >500x greater than the Rayleigh. In the PA equivalent case, the increase was ~4.5x. The difference between the Faran and Rayleigh shape

parameter *GG c/v* was ~12x for the US case and ~6x for the PA case. These changes were statistically significant ($p<0.05$).

The GG PDFs are different between the phantoms and follow the same trend in shape and scaling (figure 3). However, the physical interpretation of these differences is complex. The scale parameter *GG a* is typically related to the effective scatterer number density as well as to the scattering cross-section [24]. In the case of the Rayleigh and Faran phantoms, the number density remained the same since there were 10 beads/resolution volume of the transducer. However, the different bead sizes increased both the US backscatter and PA signal amplitude as can be seen by the enhanced brightness of images in figure 2 as well as the shift in the Faran envelope histograms towards higher signal amplitudes (figure 3). This suggests that the scaling parameter is sensitive to changes in size of scatterer/absorber and can potentially be used to monitor tissues undergoing cell death or vascular changes typically associated with tumor metabolism [3]. In addition, changes in the shape parameter *GG c/v* are often attributed to increases in the number density of scatterers. Increases in *GG c/v* in the case of the Faran phantom cannot be explained by changes in number density since the bead number density was kept the same in both cases (to the best of our efforts, but not independently confirmed). It is worth mentioning here that the randomization of the scatterers can also play a role in affecting the shape parameter. Comparing the envelope histograms of both modalities, the distribution of signal amplitudes becomes wider in the case of Faran phantoms. The GG shape parameter has been shown to significant fluctuate both due to the randomization occurring from the to treatment of cells with chemotherapy [23] as well as from the intra/inter subject variability of human skin layers [22]. This suggests that variations within the *GG c/v* parameter are perhaps sensitive enough to differentiate between heterogeneous areas within tumors imaged with US/PA thus providing localized monitoring of the spatial organization of blood vessels and cells which is an indicator of the longitudinal effectiveness of treatment.

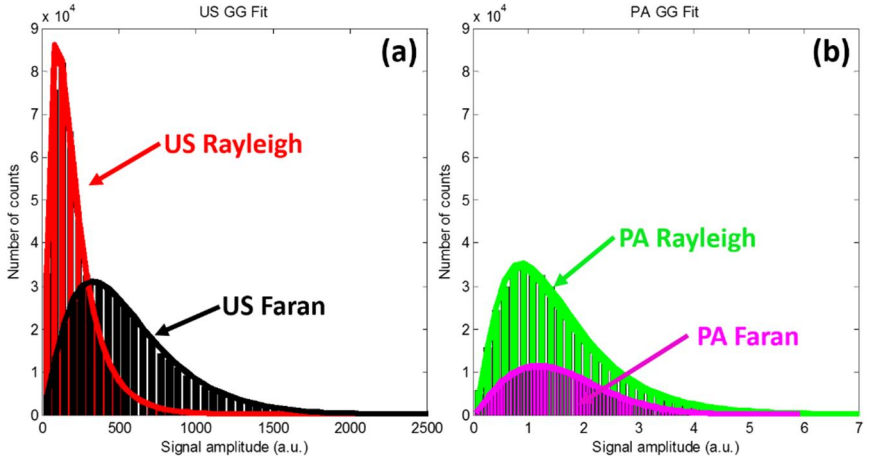

Figure 3. (a) US and (b) PA signal envelope histograms and the GG PDF fits. The GG fits shown are from 5 different ROIs within each phantom.

Table 2. Summary of the US and PA GG fit parameters and KS goodness of fit parameter. The errors represent the standard deviation of the fit parameters from 5 GG fits where each fit corresponds to a different ROI within the same phantom. The fit model is accepted if the goodness of fit KS value is smaller than CV = 0.14 for 5% significance level.

Imaging method	**US**		**PA**	
Phantom	**Rayleigh**	**Faran**	**Rayleigh**	**Faran**
GG a	0.48 ± 0.03	245.98 ± 8.0	0.35 ± 0.09	1.57 ± 0.02
GG c/v	0.037 ± 0.001	0.44 ± 0.01	0.25 ± 0.05	1.44 ± 0.01
KS	0.10 ± 0.002	0.088 ± 0.0004	0.095 ± 0.002	0.025 ± 0.001

3.3 Ultrasonic spectral parameters

The normalized RF power spectra for US and PA imaging of the phantoms are shown in figure 4. The summary of the spectral parameters extracted from the linear fits to the normalized power spectra is presented in table 3. Both US and PA

RF spectral analysis, show statistically significant changes in the ultrasonic spectral parameters as a function of scatterer/absorber size and concentration. Specifically, the US SS decreases by ~0.8x when the size of the beads increases by ~5.6 µm. The PA SS follows the same trend but the decrease is ~0.4x. This is in accordance to previous reports which have shown decreases in PA SS as a function of scattterer/absorber size in both US and PA [14], [21]. Furthermore, the SS did not change within the same phantom as different ROIs were imaged. This can be attributed to the fact that the polystyrene beads used were mono-disperse in size suggesting that the SS is a parameter which is sensitive to changes in absorber/scatterer size and not sensitive to their spatial organization. Such property of the PA SS could potentially be useful in monitoring changes that occur within tumors during angiogenesis for the purposes of monitoring the development of blood vessels and their size variations as an indicator of treatment efficacy. Moreover, the MBF is also ~10 dB higher for the Faran phantom compared to Rayleigh. This change in MBF can be attributed to the increased backscattering from the phantoms due to changes in scattering cross section.

Differences that exist between the US and PA SS are perhaps related to the mechanism of signal generation from the same collection of scatterers and absorbers. In US imaging, the detected signals are a result of the backscattering contributions from each bead. This is directly affected by the transmitted pulse properties (i.e. frequency and duration) as well as the resolution of the imaging system [13]. In PA, when uniform illumination is achieved, the generated PA signal depends directly upon the physical properties of the absorber such as size, density and speed of sound [18]. Given the broadband nature of PA signals, it results in a wider usable bandwidth as observed in the case of PA spectra shown in figure 4(b).

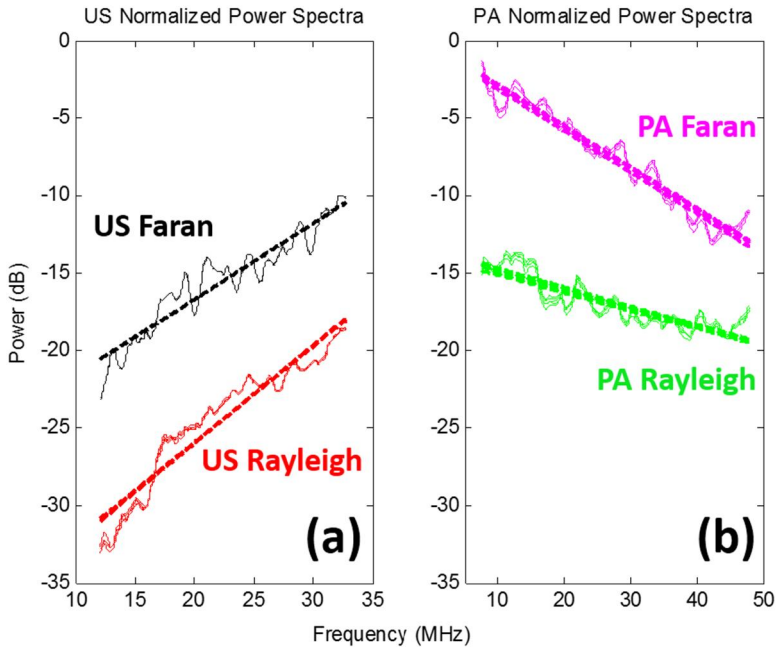

Figure 4. (a) US and (b) PA normalized power spectra within the -6 dB transducer bandwidth. The spectra and linear fits shown are from 5 different ROIs within each phantom.

Table 3. Summary of the US and PA SS and MBF spectral parameters. The errors represent the standard deviation of spectral parameters parameters from 5 linear fits where each fit corresponds to a different ROI within the same phantom.

Imaging method	**US**		**PA**	
Phantom	**Rayleigh**	**Faran**	**Rayleigh**	**Faran**
SS (dB/MHz)	0.66 ± 0.004	0.51 ± 0.001	-0.18 ± 0.002	-0.25 ± 0.002
MBF (dB)	-24.75 ± 0.02	-15.72 ± 0.006	-16.43 ± 0.2	-6.03 ± 0.1

4. CONCLUSIONS

Combining US/PA envelope statistics with ultrasonic spectral parameters can potentially be used to characterize biological tissues in the presence of many sub-resolution sources of sound. Envelope statistics are likely sensitive to changes in number density of scatterer/absorbers in to their addition to the spatial organization. The GG fit parameters to PA signal envelope histograms for Faran-type absorbers (7.36 μm) were nearly 350% higher than Rayleigh-type counterpart (1.77 μm) while the PA SS decreased by ~40%. By combining the fit parameters of the signal envelope histogram to the ultrasonic spectral parameters, it might be possible to obtain an overall mapping of the size and spatial organization of cellular sources of sound from tissues.

REFERENCES

[1] Wang, L. V. and Hu, S., "Photoacoustic tomography: in vivo imaging from organelles to organs," Science 335, 1458-1462 (2012).

[2] Strohm, E. M., Berndl, E. S. L. and Kolios, M. C., "Probing red blood cell morphology using high-frequency photoacoustics," Biophy. J. 105, 1-9 (2013).

[3] Hu, S. and Wang, L. V., "Photoacoustic imaging and characterization of the microvasculature," J. Biomed. Opt. 15(1), 011101-1-15 (2010).

[4] Levi, J., et al "Molecular photoacoustic imaging of follicular thyroid carcinoma," Clin. Cancer Res. 19(6), 1494-1502 (2013).

[5] Mallidi, S., Luke, G. P. and Emelianov, S., "Photoacoustic imaging in cancer detection, diagnosis and treatement guidance," Trends. Biotechnol. 29, 213-221 (2011).

[6] Erpelding, T. N., et al "Three-dimensional photoacoustic imaging with a clinical two-dimensional matrix ultrasound transducer," Proc. SPIE 7899, A1-6 (2011).

[7] Needles, A. et al "Development and initial application of a fully integrated photoacoustic micro-ultrasound system," IEEE T. Ultrason. Ferr. 60(5), 888-897 (2013).

[8] Taruttis, A., Morscher, S., Burton, N. C., Razanky, D. and Ntziachristos, V., "Fast multispectral optoacoustic tomography (MSOT) for dynamic imaging of pharmacokinetics and biodistribution in nultiple organs," PLoS ONE 7(1), 1-6 (2012).

[9] Ermilov, S., et al "Detection and noninvasive diagnostics of breast cancer with 2-color laser optoacoustic imaging system," Proc. SPIE 6437, 6437-A-1-6 (2007).

[10] Heijblom, M., et al "Visualizing breast cancer using the Twente photoacoustic mammoscope What do we learn from twelve new patient measurements?," Opt. Express 20(11), 11582-11597 (2012).

[11] Ku, G., Wang, X., Xie, X., Stoica, G. and Wang, L. V., "Imaging of tumor angiogenesis in rat brains in vivo by photoacoustic tomography," Appl. Optics 44(5), 770-775 (2005).

[12] Wang, L., Maslov, K. and Wang, L. V., "Single-cell label-free photoacoustic flowoxigraphy in vivo," P. Natl. Acad. Sci. USA 110(15), 5759-5764 (2013).

[13] Szabo, T. L. [Diagnostic Ultrasound Imaging: Inside Out], Elsevier Academic Press, New York, 97-135 (2004).

[14] Lizzi, F. L., Greenbaum, M., Feleppa, E. J., Elbaum, M. and Coleman, D. J., "Theoretical framework for spectrum analysis in ultrasound tissue characterization," J. Acoust. Soc. Am. 73(4), 1366-1373 (1983).

[15] Shankar, P. M., "A general statistical model for ultrasonic backscattering from tissue," IEEE T. Ultrason. Ferr. 47(3), 727-736 (2000).

[16] Mamou, J. and Oelze, M. L., [Quantitative ultrasound in soft tissues] Springer, New York & London, 95-115 (2013).

[17] Sadeghi-Naini, A., et al "Quantitative ultrasound evaluation of tumour cell death response in locally advanced breast cancer patients receiving chemotherapy," Clin. Cancer Res. 19(8), 2163-2174 (2013).

[18] Wang, L. V., [Photoacoustic Imaging and Spectroscopy], CRC Press, Boca Raton, 3-17 (2009).

[19] Strohm, E. M., Berndl, E. S. L. and Kolios, M. C., "High frequency label-free photoacoustic microscopy of single cells," Photoacoustics 1, 49-53 (2013).

[20] Hysi, E., Saha, R. K. and Kolios, M. C., "On the use of photoacoustics to detect red blood cell aggregation," Biomed. Opt. Express 3(9), 2326-2338 (2012).

[21] Hysi, E., Saha, R. K. and Kolios, M. C., "Photoacoustic ultrasound spectroscopy for the assessment of red blood cell aggregation and oxygenation," J. Biomed. Opt. 17(12), 125006-1-10 (2012).

[22] Raju, B. I. and Srinivasan, M. A., "Statistics of envelope of high-frequency ultrasonic backscatter from human skin in vivo," IEEE T. Ultrason. Ferr. 49(7), 871-882 (2002).
[23] Tunis A. S., et al "Monitoring structural changes in cells with high frequency ultrasound signal statistics," Ultrasound Med. Biol. 31(8), 1041-1049 (2005).
[24] Tunis, A. S., et al "Using high frequency ultrasound envelope statistics to determine scatter number density in dilute cell solutions," Proc. IEEE IUS 2, 878-881 (2005).